Front. Environ. Sci. Eng. 2022, 16(10): 125
https://doi.org/10.1007/s11783-022-1557-0

RESEARCH ARTICLE

# Effect of Cu-ZSM-5 catalysts with different CuO particle size on selective catalytic oxidation of N,N-Dimethylformamide

**Xin Xing[1], Na Li[2], Dandan Liu[1], Jie Cheng (✉)[2], Zhengping Hao[2]**

1 College of Environmental Science and Engineering, Taiyuan University of Science and Technology, Taiyuan 030024, China
2 National Engineering Laboratory for VOCs Pollution Control Material & Technology, Research Center for Environmental Material and Pollution Control Technology, University of Chinese Academy of Sciences, Beijing 101408, China

## HIGHLIGHTS

- A series of Cu-ZSM-5 catalysts were tested for DMF selective catalytic oxidation.
- Cu-6 nm samples showed the best catalytic activity and $N_2$ selectivity.
- Redox properties and chemisorbed oxygen impact on DMF catalytic oxidation.
- Isolated $Cu^{2+}$ species and weak acidity have effects on the generation of $N_2$.

## GRAPHIC ABSTRACT

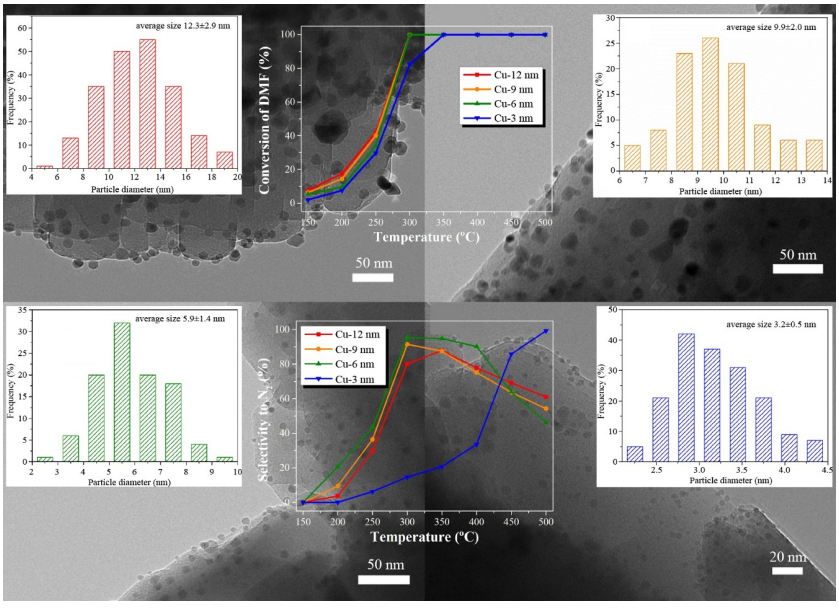


## ARTICLE INFO

*Article history:*
Received 12 October 2021
Revised 31 December 2021
Accepted 5 January 2022
Available online 20 February 2022

*Keywords:*
N, N-Dimethylformamide
Selective catalytic oxidation
Cu-ZSM-5
CuO particle size

## ABSTRACT

N,N-Dimethylformamide (DMF), a nitrogen-containing volatile organic compound (NVOC) with high emissions from the spray industry, has attracted increasing attention. In this study, Cu-ZSM-5 catalysts with different CuO particle sizes of 3, 6, 9 and 12 nm were synthesized and tested for DMF selective catalytic oxidation. The crystal structure and physicochemical properties of the catalyst were studied by various characterization methods. The catalytic activity increases with increasing CuO particle size, and complete conversion can be achieved at 300–350 °C. The Cu-12 nm catalyst has the highest catalytic activity and can achieve complete conversion at 300 °C. The Cu-6 nm sample has the highest $N_2$ selectivity at lower temperatures, reaching 95% at 300 °C. The activity of the catalysts is determined by the surface CuO cluster species, the bulk CuO species and the chemisorbed surface oxygen species. The high $N_2$ selectivity of the catalyst is attributed to the ratio of isolated $Cu^{2+}$ and bulk CuO species, and weak acidity is beneficial to the formation of $N_2$. The results in this work will provide a new design of NVOC catalytic oxidation catalysts.



## 1 Introduction

Increasing attention has been given to the treatment of nitrogen-containing volatile organic compounds (NVOCs)

✉ Corresponding author
E-mail: jiecheng@ucas.ac.cn

because the secondary pollutant $NO_x$ is facing strict environmental regulations. NVOCs are emitted from various sources, such as the petrochemical, pharmaceutical, synthetic leather, coating and other industries (Zhang et al., 2016b; He et al., 2019). Common NVOCs are mainly amines, amides, nitriles, nitrates and other pollutants. NVOCs generally have pungent odors, which could cause harm to the human body through inhalation into the respiratory system or directly contact with the skin (Ma et al., 2018). N,N-Dimethylformamide (DMF) is an amide that is a typical NVOC. DMF is an inexpensive and easily accessible organic solvent, and it is extensively used in the industrial processes. Many reactions involve the decomposition of DMF into CO, which is then used to carry out subsequent reactions (Feng and Li, 2017). However, the degradation of DMF and subsequent secondary pollution are rarely studied.

The control methods of VOC emissions can be divided into recovery and destruction, which include adsorption, absorption, condensation, membrane separation, combustion, catalytic oxidation and photocatalysis (Kim et al., 2017; Zhang et al., 2017; Li et al., 2020). For the treatment of NVOCs, the key point is the control of the conversion of N atoms, which need to be converted to $N_2$ rather than other nitrogen-containing byproducts. Among these methods, selective catalytic oxidation is an effective degradation method for NVOCs. It requires lower reaction temperatures and can achieve the complete degradation of NVOCs. Additionally, NVOCs can be converted to $CO_2$, $H_2O$ and $N_2$, avoiding the generation of the secondary pollutant $NO_x$ and more hazardous pollutants such as HCN (Nanba et al., 2004; Nanba et al., 2007).

In recent years, some researchers have studied the catalytic degradation of NVOCs. Ning et al. reported that Cu-Mn-O exhibited excellent catalytic performance for the decomposition of HCN at low temperatures, and in situ DRIFTS has been carried out to study the intermediate products in the reaction process (Liu et al., 2017). Nanba et al. studied the effect of supports on Ag catalysts for acrylonitrile decomposition (Nanba et al., 2008). Zhang et al. found that perovskite catalysts ($LaFe_{0.8}Cu_{0.2}O_3$) presented the best conversion and $N_2$ selectivity for the selective catalytic oxidation of acrylonitrile and revealed that surface-adsorbed oxygen played an important role in this reaction at low temperatures (Zhang et al., 2016a). Chen et al. synthetized Cu/SBA-15 catalysts and tested them for $CH_3CN$ catalytic oxidation. This sample exhibited almost complete conversion of $CH_3CN$ with a $N_2$ selectivity of 80% at $T > 350$ °C (Zhang et al., 2014). It was observed that the Pd/SBA-15-r sample possessed good catalytic performance of *n*-butylamine, which could be due to the dispersion of Pd active sites (Ma et al., 2020). Zhou et al. proposed that the large pore volume of pillared clay is beneficial to the dispersion of CrCe active phases. This catalyst has excellent catalytic performance for the degradation of *n*-butylamine (Huang et al., 2010). At present, few research teams have focused on the catalytic degradation of DMF. DMF is often emitted in the coating and pharmaceutical industries, and the molecular structure of DMF has unique characteristics.

In this work, Cu-ZSM-5 catalysts with different sizes of CuO particles were synthesized and used for the selective catalytic oxidation of DMF. The structure and physicochemical properties of these catalysts will be discussed in terms of the following characterizations: high-resolution transmission electron microscopy (HR-TEM), X-ray diffraction (XRD), $^{27}Al$ magic angle spinning nuclear magnetic resonance ($^{27}Al$ MAS NMR), $H_2$ temperature-programmed reduction ($H_2$-TPR), X-ray photoelectron spectroscopy (XPS), temperature-programmed desorption of ammonia ($NH_3$-TPD), and Electron paramagnetic resonance (EPR). Various characterization techniques were used to study the effect of CuO particle size on the formation of Cu species, acid sites and redox properties, which further affected the catalytic activity and $N_2$ selectivity of DMF catalytic oxidation.

## 2 Experimental

### 2.1 Preparation of catalysts

H-ZSM-5(25) zeolite was purchased from the Nankai University Catalyst Plant (China). Cupric chloride ($CuCl_2 \cdot 2H_2O$, Analytical Reagent), sodium borohydride ($NaBH_4$, Analytical Reagent), sodium citrate ($Na_3C_6H_5O_7$, Analytical Reagent), polyvinyl alcohol (PVA, Analytical Reagent), and ethanol ($CH_3CH_2OH$, Analytical Reagent) were purchased from Sinopharm Chemical Regent Co., Ltd., China.

The preparation of Cu-12 nm samples involved the following steps: 4 g of H-ZSM-5(25) was dispersed in 300 mL deionized water and ultrasonicated for 10 min. Then, 2 mL of aqueous $CuCl_2$ solution ($1.69 \times 10^5$ mg/L) was added to the above solution and stirred for 30 min. After that, 2 mL of $Na_3C_6H_5O_7$ ($4.25 \times 10^5$ mg/L) was added, and the mixture was stirred for 30 min. Subsequently, the solution was injected with 2 mL $NaBH_4$ ( $3.33 \times 10^5$ mg/L) and stirred for 2 h. Finally, the sample was washed with deionized water and ethanol and then dried at 50 °C for 12 h.

The synthesis of the Cu-9 nm sample was similar to that of the Cu-12 nm sample. In the process of synthesizing the Cu-9 nm catalyst, the concentration of $Na_3C_6H_5O_7$ was half that of Cu-12 nm.

The preparation of Cu-6 nm was different from that of Cu-12 nm and Cu-9 nm. The Cu-6 nm sample was prepared by colloidal deposition as described in the related literature (Wang et al., 2017). Typically, 200 mL of ethanol was added to a 500 mL round bottom flask and heated to 60 °C. Then, $CuCl_2$ solution ($1.69 \times 10^5$ mg/L,

2 mL) and $Na_3C_6H_5O_7$ ($2.13 \times 10^5$ mg/L, 48 mL) complexing agent were added in turn. After condensation and reflux for 30 min, the color of the solution changed. Next, the H-ZSM-5(25) zeolite was added into the flask and stirred continuously for 2 h. The product was washed several times with deionized water and dried at 50 °C for 12 h.

The preparation of Cu-3 nm differed slightly from that of Cu-6 nm. Deionized water (50 mL) was added to a 250 mL round bottom flask and heated to 60 °C. Then, $CuCl_2$ and PVA solution (0.532 g, 48 mL) was added to the flask. The remaining steps were the same as those in the above synthesis of Cu-6 nm.

### 2.2 Catalytic activity evaluation

The DMF catalytic oxidation reaction was investigated in a quartz fixed bed reactor with an inner diameter of 8 mm and an outer diameter of 10 mm. Each catalyst was pressed and sieved to 20–40 mesh and then placed in the middle of the reactor. The reaction gases were composed of DMF and $O_2$ with helium as the equilibrium gas, and DMF entered the mixed gas with He, which was used as the carrier gas. The reaction temperature ranged from 150 to 500 °C, and the gas hourly space velocity (GHSV) of the whole process was maintained at 18000 $h^{-1}$. Notably, heat preservation was necessary throughout the gas circuit. The exhaust gases were detected by gas chromatography (7890A, Agilent, USA) and FTIR spectroscopy (Multi-Gas 2030, MKS, USA). The calculation details of the catalytic activity evaluation are as follows (Eqs. (1–3)):

$$\text{DMF conversion}(\%) = \frac{\text{DMF(in)} - \text{DMF(out)}}{\text{DMF(in)}} \times 100, \quad (1)$$

$$\text{CO/CO}_2\text{ selectivity}(\%) = \frac{\text{CO/CO}_2(\text{vol.}\%)}{\text{Total product C (vol.}\%)} \times 100, \quad (2)$$

$$\text{NO/N}_2\text{O/N}_2\text{ selectivity}(\%) = \frac{\text{NO/N}_2\text{O/N}_2(\text{vol.}\%)}{\text{Total product N(vol.}\%)} \times 100. \quad (3)$$

### 2.3 Characterization of catalysts

HR-TEM images were performed on A JEM-2010F (Japan) transmission electron microscope (200 kV).

XRD patterns were obtained with an X'Pert PRO (PANalytical, the Netherlands) diffractometer using Cu K$\alpha$ radiation, and a scanning speed of 7°/min.

$H_2$-TPR were performed by a Micromeritics Chemisorb 2920 (USA). The catalyst (50 mg) was pretreated under Ar from room temperature to 300 °C and held for 1 h. The TPR profiles were obtained by passing a 5 vol.% $H_2$/Ar flow (50 mL/min) through the pretreated samples. The reduction temperature was increased from room temperature to 900 °C. The hydrogen concentration in the effluent was continuously monitored by a thermal conductivity detector (TCD).

XPS was measured on a Thermo ESCALAB 250 instrument (USA), using a standard Al Kα X-ray source.

$^{27}$Al MAS NMR spectra were carried out at room temperature on a Bruker Advance 400 spectrometer (Germany).

$NH_3$-TPD was conducted in Micromeritics Chemisorb 2920 (USA) equipped with a TCD. Prior to each TPD run, the catalyst (100 mg) was pretreated under a helium flow at 300 °C for 1 h, and then the sample need to be naturally cooled to room temperature. Subsequently, the catalyst adsorbed $NH_3$ for 30 min under a 5 vol.% $NH_3$/He of 50 mL/min. Then, helium gas was fed into the reactor at 50 mL/min for 30 min to purge any residual $NH_3$. The catalyst was then heated to 900 °C with a heating rate of 10 °C/min under a helium flow.

EPR spectra were performed at −160 °C using a JES FA 200 spectrometer (Japan).

## 3 Results and discussion

### 3.1 HR-TEM and XRD

TEM images of the catalysts and the corresponding size distribution of CuO nanoparticles are shown in Fig. 1. The TEM images show that the ZSM-5 supports had a sheet-like morphology and that the CuO particles were uniformly distributed on ZSM-5. Based on the size distribution, four different sizes of ZSM-5-supported CuO were obtained, and they were denoted as Cu-12 nm, Cu-9 nm, Cu-6 nm and Cu-3 nm.

XRD analysis was used to identify the phase structure of the catalysts, as shown in Fig. 2. In the patterns of all the catalysts, the planes (1 0 1), (2 0 0), (0 2 0), (3 3 2), (0 5 1) and (3 0 3) of ZSM-5 (JCPDS 44-0003) could be observed at 7.9°, 8.8°, 8.9°, 23.1°, 23.3° and 23.9°, respectively (Dou et al., 2015; Lai et al., 2015). The catalysts modified by Cu retain the structure of ZSM-5 itself, which shows that the introduction of copper has almost no effect on the support structure of ZSM-5. The (1 1 −1), (1 1 1) and (2 0 −2) planes of CuO (JCPDS 45-0937) could also be observed at 35.5°, 38.7° and 48.7°, respectively (Fan et al., 2013; Liu et al., 2016). Cu-3 nm exhibited an extremely small CuO peak because the intensity of the (1 1 1) and (1,1,1) planes was smaller than that of the other samples. Additionally, as the Cu nanoparticles increased, the corresponding peaks of the (1 1 −1) and (1 1 1) planes of CuO increased, showing that the dispersity of copper decreased and the CuO species formed aggregates.

### 3.2 Catalytic activity

The characteristic reaction temperatures ($T_{10}$, $T_{50}$ and $T_{90}$) are shown in Table 1. All the characteristic temperature ($T_{10}$, $T_{50}$ and $T_{90}$) decreased with the increase of CuO particles, indicating that the catalyst with larger CuO

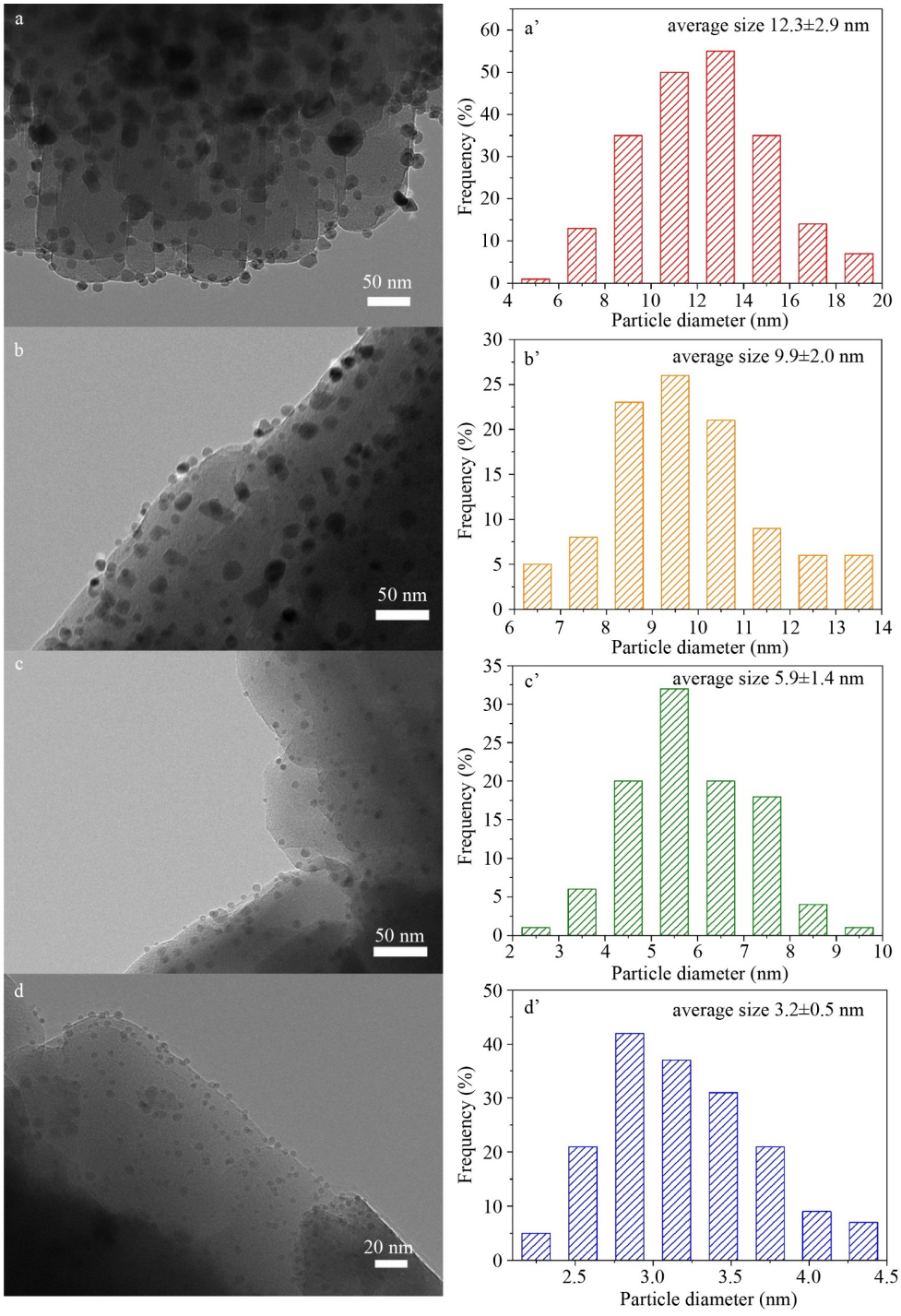


**Fig. 1** TEM images of Cu-ZSM-5 catalysts: (a) Cu-12 nm, (b) Cu-9 nm, (c) Cu-6 nm and (d) Cu-3 nm and the corresponding particle size distributions of Cu-ZSM-5 catalysts: (a') Cu-12 nm, (b') Cu-9 nm, (c') Cu-6 nm and (d') Cu-3 nm.

particles has better conversion. The catalytic conversion of Cu-ZSM-5 catalysts with different CuO sizes is shown in Fig. 3(a). Cu-12 nm exhibited the highest conversion of DMF during 150–500 °C, and the temperature at which DMF was completely converted was 300 °C, which was same as that of Cu-9 nm and Cu-3 nm. Notably, the catalytic performance of Cu-3 nm was lower than that of other samples, and the DMF could be completely converted at 350 °C. The order of DMF conversion from high to low was Cu-12 nm > Cu-9 nm > Cu-6 nm > Cu-3 nm. Interestingly, the conversion of DMF was associated with the size of the CuO particles, and the catalytic activity of DMF increased with the increase in CuO particle size.

The CO and $CO_2$ selectivity are shown in Figs. 3(b) and 3(c). In the formation of CO, the CO selectivity of Cu-12 nm, Cu-9 nm and Cu-6 nm first increased and then decreased as the temperature increased. There was almost no CO formation at T > 300 °C over these samples.

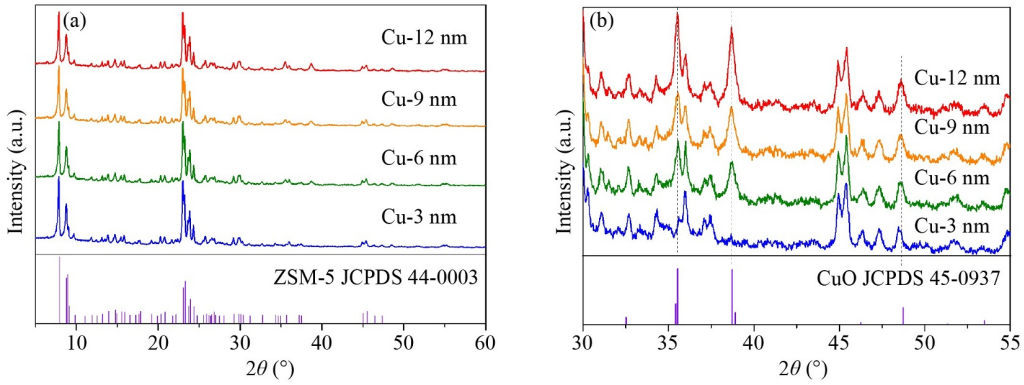


**Fig. 2** XRD patterns (a) and locally amplified XRD patterns (b) of Cu-12 nm, Cu-9 nm, Cu-6 nm and Cu-3 nm.

**Table 1** Characteristic reaction temperatures ($T_{10}$, $T_{50}$ and $T_{90}$), composition of Cu species and O species calculated by XPS results

| Samples | $T_{10}$ (°C) | $T_{50}$ (°C) | $T_{90}$ (°C) | Isolated $Cu^{2+}$/bulk CuO | $O_{ads}/O_{latt}$ |
|---|---|---|---|---|---|
| Cu-12 nm | 161 | 256 | 291 | 2.12 | 2.17 |
| Cu-9 nm | 172 | 259 | 291 | 2.42 | 1.57 |
| Cu-6 nm | 198 | 262 | 292 | 3.28 | 1.32 |
| Cu-3 nm | 205 | 270 | 321 | 1.62 | 1.23 |

However, the formation of CO was detected across the whole temperature range of the Cu-3 nm catalyst, and the selectivity of CO was as high as 40%. In the formation of $CO_2$, the $CO_2$ selectivity increased with increasing temperature. At 350 °C, the $CO_2$ selectivity of Cu-12 nm, Cu-9 nm and Cu-6 nm reached 100%. For the Cu-3 nm sample, the selectivity of $CO_2$ was only approximately 80% at 500 °C, which indicated that the oxidation activity of the Cu-3 nm catalyst was poorer than that of the other samples.

The results of the catalytic selectivity of N-containing products (NO, $N_2O$ and $N_2$) are presented in Figs. 3(d)–3(f). The selectivity to NO could be divided into two categories. When the temperature was lower than 300 °C, the NO selectivity increased first and then decreased with increasing temperature, and there was no formation of NO at approximately 300 °C. At $T$ > 300 °C, the production of NO increased rapidly, and the selectivity to NO increased with increasing temperature. For $N_2O$, the selectivity for $N_2O$ first increased and then decreased across the whole temperature range of 150–500 °C, and it began to slowly decline after 300–350 °C. At 500 °C, a small amount of $N_2O$ was still present. For the Cu-12 nm, Cu-9 nm and Cu-6 nm catalysts, the selectivity for $N_2$ increased with increasing temperature until 300 °C was reached. The $N_2$ selectivity of the Cu-6 nm sample reached 95% at 300 °C (NO did not form at approximately 300 °C). The continuous increase in temperature led to a rapid decrease in $N_2$ selectivity, and the selectivity to $N_2$ was approximately 50% at 500 °C. For Cu-3 nm, the formation and variation of byproducts are different. At 350 °C, the conversion of DMF reached 100%, but the amounts of inorganic nitrogen-containing products were very small, which indicated that DMF probably transformed into other organic byproducts and needed a higher decomposition temperature to produce $CO_2$, $N_2$ and $H_2O$. When the temperature was raised above 450 °C, the $N_2$ selectivity increased rapidly; this temperature was higher than that used for other catalysts. All the results show that the oxidation activity of Cu-3 nm was lower than that of the other samples.

### 3.3 $H_2$-TPR

$H_2$-TPR was used to study the redox performance of catalysts, as shown in Fig. 4. All the samples except Cu-6 nm exhibited two reduction peaks. The peaks centered at 300–350 °C were ascribed to highly dispersed Cu species that strongly interact with ZSM-5 supports (Pereda-Ayo et al., 2014; De La Torre et al., 2016). This result indicates that some of the Cu species entered the lattice of the ZSM-5 zeolite, and the strong interactions between them made Cu reduction difficult, which led to a high reduction temperature. The peaks at approximately 155 °C were attributed to the reduction in surface-dispersed CuO, which weakly interacted with the supports, including bulk CuO species and surface CuO cluster species. The peak at 192 °C in the spectrum of Cu-6 nm was assigned to the surface CuO cluster species, and the peak at 155 °C was probably due to bulk CuO species (Wang et al., 2014).

When the size of CuO particles was small, most of them were highly dispersed and in direct contact with the carriers, which interacted strongly with the lattice of the zeolites (Zhou et al., 2004). However, the interactions between the CuO particles and the carriers became weaker due to the large size of the CuO particles. The temperatures of the second reduction peaks decreased with increasing CuO particle size, which indicated that the

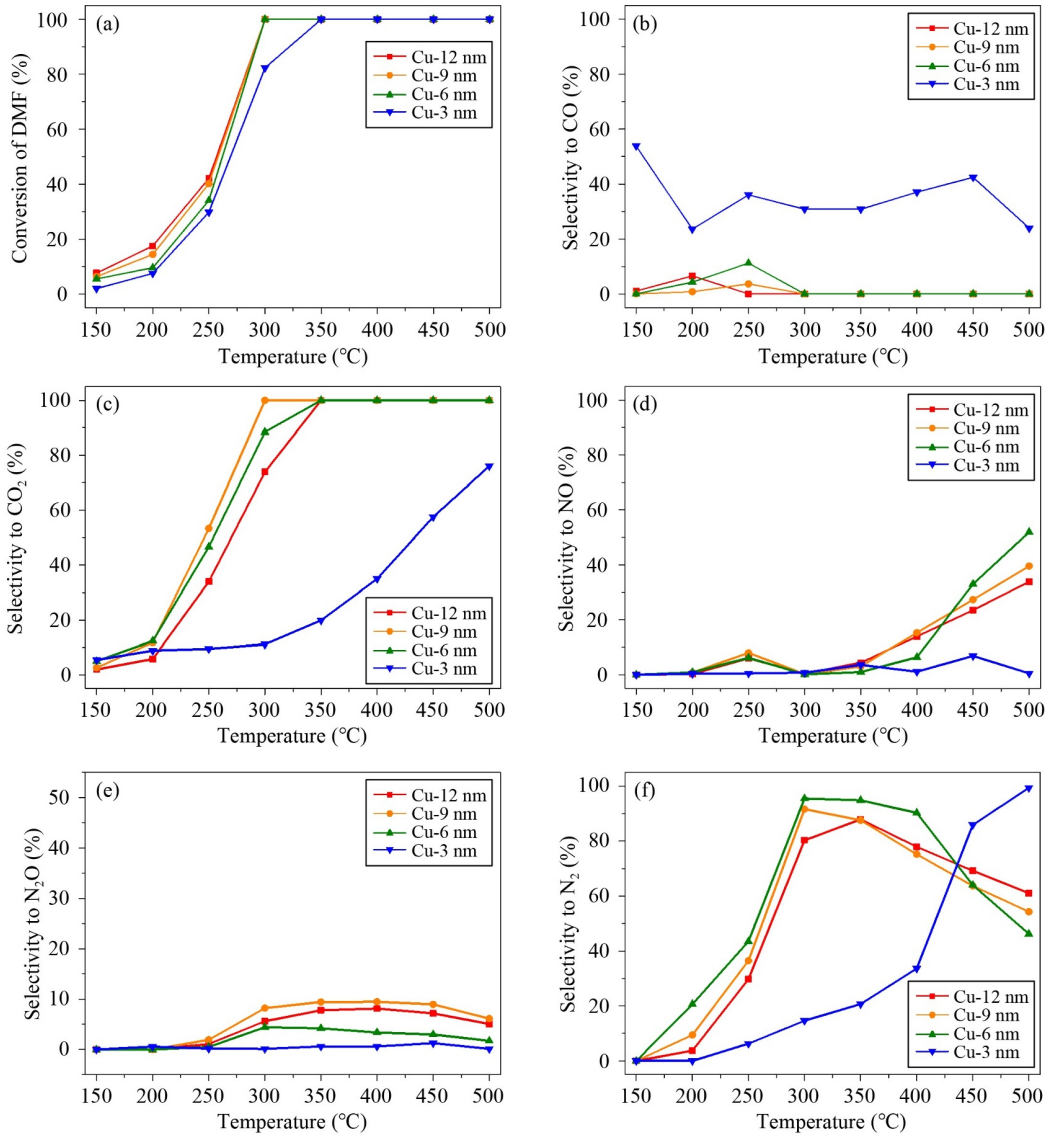


**Fig. 3** The conversion of DMF (a), the CO selectivity (b), $CO_2$ selectivity (c), NO selectivity (d), $N_2O$ selectivity (e) and $N_2$ selectivity (f) in 150–500 °C.

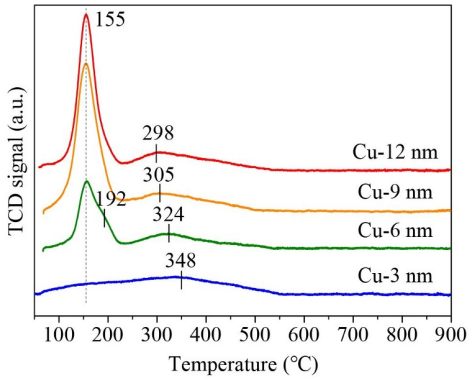


**Fig. 4** $H_2$-TPR results of Cu-12 nm, Cu-9 nm, Cu-6 nm and Cu-3 nm.

larger the particles were, the weaker the interaction between the particles and the carrier. With increasing CuO particle size, there were more particles with weaker interactions with the supports, so the peak area of low-temperature reduction was increasingly larger. The order of the peak area of the low-temperature $H_2$ reduction peaks from high to low area is Cu-12 nm > Cu-9 nm > Cu-6 nm > Cu-3 nm, which is consistent with the order of the catalytic conversion of DMF. The results indicated that the surface CuO cluster species and the bulk CuO species significantly affect the catalytic oxidation of DMF.

### 3.4 XPS

To determine the chemical valence state of copper, XPS spectra were taken and are shown in Fig. 5. Peaks at approximately 934 and 954 eV are observed, which are ascribed to Cu $2p^{3/2}$ and Cu $2p^{1/2}$, respectively (Xing et al., 2020). Two satellite peaks at 943 and 962 eV, which suggest the appearance of $Cu^{2+}$, are present. The Cu $2p^{3/2}$ peaks could be divided into two peaks: the peak at 933.4 eV

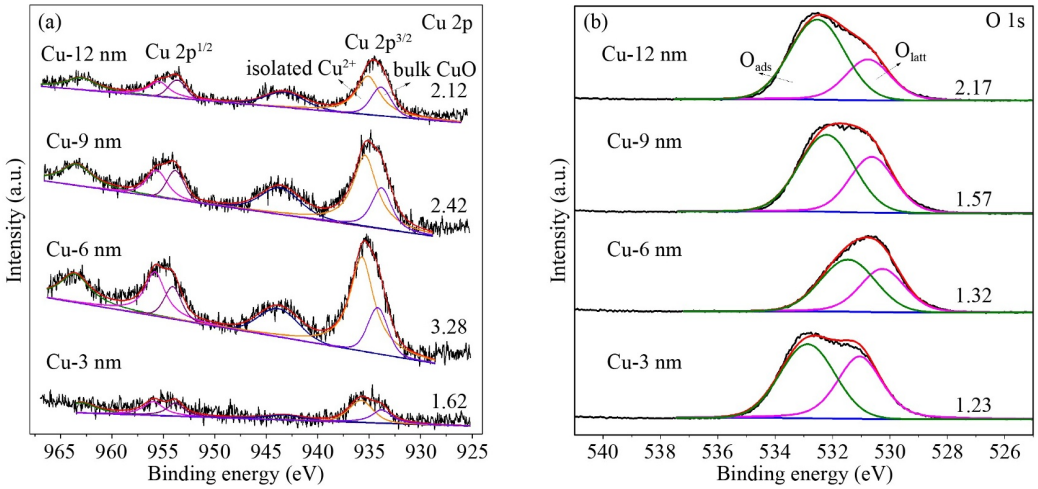


**Fig. 5** XPS spectra of Cu 2p (a) and O 1s (b) over Cu-12 nm, Cu-9 nm, Cu-6 nm and Cu-3 nm.

could be assigned to bulk CuO, and the peak at approximately 935.3 eV was attributed to highly dispersed CuO species, such as isolated $Cu^{2+}$ and oligomeric Cu-O-Cu species (Lai et al., 2015; Xue et al., 2018). The proportions of isolated $Cu^{2+}$ and bulk CuO could be calculated by the peak area of the corresponding peaks. The proportion value of Cu-6 nm was 3.28, which is highest among other samples. The order of isolated $Cu^{2+}$ and the bulk CuO ratio from high to low are as follows: Cu-6 nm > Cu-9 nm > Cu-12 nm > Cu-3 nm, which is consistent with the trend in $N_2$ selectivity of these catalysts.

Oxygen species on the surface of catalysts are usually studied by O-XPS, as shown in Fig. 5. The O 1s XPS spectra could be deconvoluted into two peaks, the first peak centered at approximately 530.5 eV corresponded to lattice oxygen species ($O_{latt}$) (He et al., 2013). Another peak at 532.6 eV was assigned to the oxygen species chemisorbed on the surface ($O_{ads}$), which are from hydroxyl species, absorbed $O_2$ and adsorbed water (Pan et al., 2017). The distribution of oxygen species could be calculated according to the peak area of each sample, as shown in Table 1. It has been shown that surface chemisorption oxygen species are more active than lattice oxygen species in catalytic oxidation reactions. The $O_{ads}/O_{latt}$ value of Cu-12 nm (2.17) was much higher than that of other catalysts, which indicated that Cu-12 nm had more chemisorbed oxygen species, which are instrumental in the catalytic oxidation of DMF to $CO_2$ and $H_2O$.

### 3.5 $^{27}$Al MAS NMR

$^{27}$Al MAS NMR spectroscopy was carried out to study the coordination status of aluminum, and the spectra of H-ZSM-5 and Cu-ZSM-5 are presented in Fig. 6(a). All samples showed a sharp dominant signal near 55 ppm, which could be ascribed to tetrahedrally coordinated Al in lattice positions (framework Al). A small peak at 0 ppm corresponded to Al in octahedral symmetry, demonstrating the presence of extra-framework Al (Zhao et al., 2019). Compared to the H-ZSM-5 supports, the integrated peak areas of the tetrahedrally coordinated Al in Cu-modified samples are calculated (see Fig. 6(b)). The peaks of the framework Al decreased after Cu modification, which might be due to dealumination or the presence of paramagnetic $Cu^{2+}$ ions (Zhang et al., 2016c). Generally, dealumination could be simply detected by $^{27}$Al MAS NMR because the characteristic peak appears at 0 ppm. Only the Cu-3 nm sample exhibited a peak at 0 ppm, which shows that a certain degree of dealumination occurred in this sample. The reason for the decrease in the peak area of the other samples was the presence of $Cu^{2+}$ ions. This also implies that Cu loading on ZSM-5 destroyed the coordination environment of framework Al species, leading to a decrease in the symmetry of some framework Al, so the signal decreased in the NMR test.

### 3.6 $NH_3$-TPD

Temperature programmed desorption of ammonia ($NH_3$-TPD) is a common method of acid measurement that can be used to determine the acidity and acid site distribution of catalysts. Figure 7 shows the $NH_3$-TPD profiles of the samples. Three distinct desorption peaks appear at 100–900 °C, indicating that there are three acid sites with different strengths. The desorption peaks below 150 °C were attributed to $NH_3$ adsorbed on the weakly acidic sites. The desorption peaks at 150–300 °C were assigned to the desorption of $NH_3$ on the intermediate strength acid sites. The peaks centered at approximately 400 °C corresponded to the strong acid sites (Blanch-Raga et al., 2016; Luo et al., 2018). In addition, the $NH_3$ desorption temperatures of Cu-12 nm were higher than those of other samples, which indicates that this catalyst was more acidic than the other catalysts. Its $NH_3$ desorption area was the largest, showing that this sample had more acidic sites. In contrast, the acidity of Cu-3 nm was weaker, and the desorption temperatures were lower than those of the other three samples. According to the desorption temperature, the order of acidity from weak to strong is Cu-3 nm < Cu-6 nm < Cu-9 nm < Cu-12 nm.

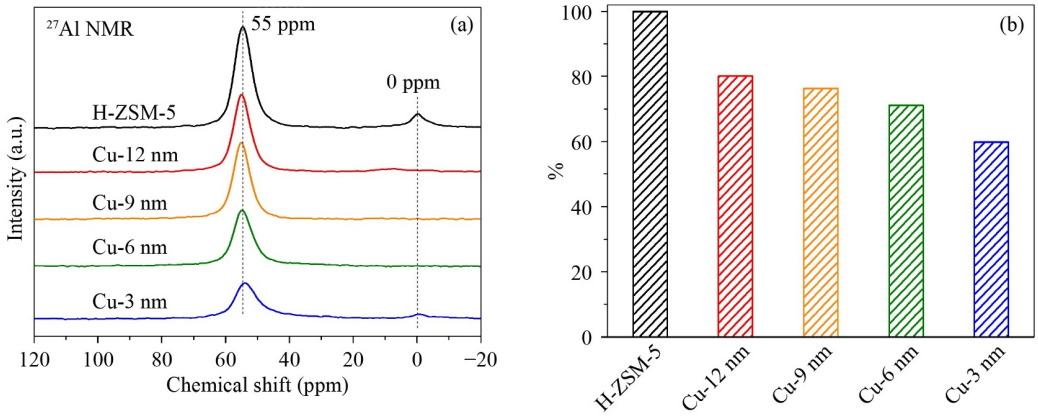


**Fig. 6** (a) $^{27}$Al MAS NMR spectra of Cu-12 nm, Cu-9 nm, Cu-6 nm and Cu-3 nm, (b) Integrated $^{27}$Al peak area of 55 ppm.

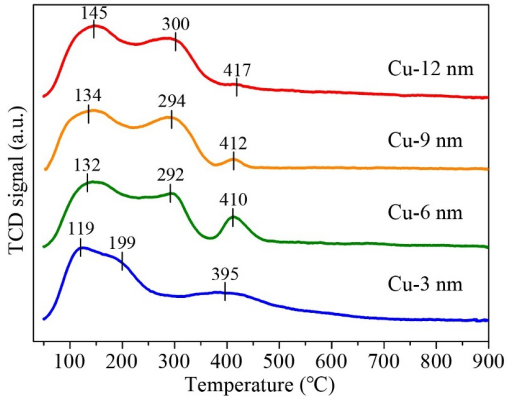


**Fig. 7** $NH_3$-TPD results of Cu-12 nm, Cu-9 nm, Cu-6 nm and Cu-3 nm.

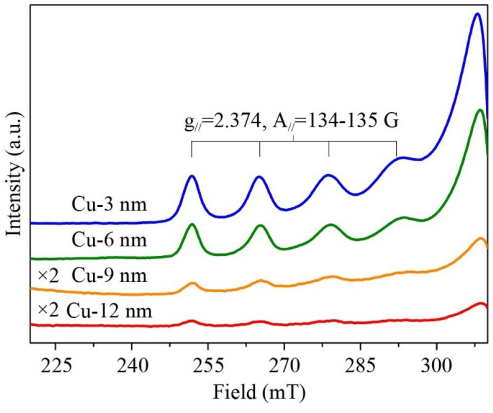


**Fig. 8** EPR results of Cu-12 nm, Cu-9 nm, Cu-6 nm and Cu-3 nm.

### 3.7 EPR

To understand the coordination of copper species, we applied EPR technology to characterize the Cu-ZSM-5 catalysts. EPR was highly effective in identifying isolated $Cu^{2+}$ species (Giordanino et al., 2013). As shown in Fig. 8, all the Cu-ZSM-5 catalysts with different CuO particle sizes exhibited four splitting features due to the hyperfine coupling between the unpaired 3d electron and the nuclear spin of copper (Liu et al., 2011). The $g$ and $A$ parameters ($g_{//}$ = 2.374, $A_{//}$ = 134–135 G) were assigned to isolated $Cu^{2+}$ species in tetragonally distorted octahedral coordination of oxygen-containing ligands (Yashnik et al., 2012). These ions seemed to be stabilized on cation-exchange positions of the ZSM-5 support (Yashnik and Ismagilov, 2015). All the materials contained isolated $Cu^{2+}$ species. However, when the particle size of CuO was larger than 6 nm, the characteristic signals and splitting features of $Cu^{2+}$ cations obviously weakened (Cu-9 nm and Cu-12 nm). This result indicates that the number of isolated $Cu^{2+}$ species decreased with increasing CuO particle size, and the main Cu species of the Cu-9 nm and Cu-12 nm catalysts could have been oligomeric Cu-O-Cu species or bulk CuO.

Through the activity tests and characterization, the following preliminary conjecture was obtained. The order of DMF conversion from high to low was Cu-12 nm > Cu-9 nm > Cu-6 nm > Cu-3 nm, the temperature at which conversion was complete ranged from 300–350 °C. The peak areas of the low temperature $H_2$ reduction peak from high to low were in the order of Cu-12 nm > Cu-9 nm > Cu-6 nm > Cu-3 nm. The $O_{ads}/O_{latt}$ value of Cu-12 nm was much higher than that of the other catalysts. This result indicated that the surface CuO cluster species, bulk CuO species and chemisorbed oxygen species are instrumental in the catalytic oxidation of DMF to $CO_2$ and $H_2O$. Without considering the total conversion temperature, the order of $N_2$ selectivity from high to low is Cu-3 nm > Cu-6 nm > Cu-9 nm > Cu-12 nm. This result is consistent with the order of isolated $Cu^{2+}$ content from EPR characterization. In addition, the catalyst with weak acidity has higher $N_2$ selectivity. These results indicate that isolated $Cu^{2+}$ species and acidic sites may be important active sites for controlling the selective conversion of N to $N_2$.

## 4 Conclusions

A series of Cu-ZSM-5 samples with different CuO particle sizes of 3, 6, 9 and 12 nm were synthesized and evaluated for DMF selective catalytic oxidation. All the

catalysts could achieve the complete conversion of DMF at 300–350 °C, and the catalyst with large CuO particles (Cu-12 nm) had the highest activity. The catalytic activity of DMF conversion was governed by redox properties and chemisorbed oxygen species. Significantly, the $N_2$ selectivity increased with decreasing CuO particle size. Cu-3 nm exhibited the highest $N_2$ selectivity, which exceeded 98% at 500 °C, but its catalytic activity was poor compared to those of the other samples. The Cu-6 nm catalyst showed good catalytic performance with a total conversion temperature and 95% $N_2$ selectivity at 300 °C. According to the characterization of these catalysts, catalysts with smaller CuO particles had a higher content of isolated $Cu^{2+}$ species. Additionally, the samples with smaller CuO particles were less acidic than the other samples. Hence, both isolated $Cu^{2+}$ species and weakly acidic sites have important effects on the formation of $N_2$. The results reported in this paper have guiding significance for the practical application of catalytic DMF degradation materials.

**Acknowledgements** This work is financially supported by the R&D Program of Beijing Municipal Education Commission (China) (No. KJZD20191443001), Beijing Municipal Science and Technology Commission (China) (No. Z181100000118003), the Key R&D Program of Shanxi Province (China) (No. 201903D311006), the Doctoral research start up fund project of Taiyuan University of science and technology (China) (Nos. 20202053 and 20192039), Research Support for Outstanding Doctors in Shanxi (China) (Nos. 20192043 and 20212060) and Scientific and Technological Innovation Programs of Higher Education Institutions in Shanxi (China) (Nos. 2021L311 and 2019L0030).

## References

Blanch-Raga N, Palomares A E, Martínez-Triguero J, Valencia S (2016). Cu and Co modified beta zeolite catalysts for the trichloroethylene oxidation. Applied Catalysis B: Environmental, 187: 90–97

De La Torre U, Urrutxua M, Pereda-Ayo B, González-Velasco J R (2016). On the Cu species in Cu/beta catalysts related to De$NO_x$ performance of coupled NSR-SCR technology using sequential monoliths and dual-layer monolithic catalysts. Catalysis Today, 273: 72–82

Dou B, Lv G, Wang C, Hao Q, Hui K (2015). Cerium doped copper/ZSM-5 catalysts used for the selective catalytic reduction of nitrogen oxide with ammonia. Chemical Engineering Journal, 270: 549–556

Fan S, Xue J, Yu T, Fan D, Hao T, Shen M, Li W (2013). The effect of synthesis methods on Cu species and active sites over Cu/SAPO-34 for $NH_3$-SCR reaction. Catalysis Science & Technology, 3(9): 2357–2364

Feng X, Li Z (2017). Photocatalytic promoting dimethylformamide (DMF) decomposition to in-situ generation of self-supplied CO for carbonylative Suzuki reaction. Journal of Photochemistry and Photobiology A Chemistry, 337: 19–24

Giordanino F, Vennestrøm P N, Lundegaard L F, Stappen F N, Mossin S, Beato P, Bordiga S, Lamberti C (2013). Characterization of Cu-exchanged SSZ-13: A comparative FTIR, UV-Vis, and EPR study with Cu-ZSM-5 and Cu-β with similar Si/Al and Cu/Al ratios. Dalton Transactions (Cambridge, England), 42(35): 12741–12761

He C, Cheng J, Zhang X, Douthwaite M, Pattisson S, Hao Z (2019). Recent advances in the catalytic oxidation of volatile organic compounds: A review based on pollutant sorts and sources. Chemical Reviews, 119(7): 4471–4568

He C, Yu Y, Chen C, Yue L, Qiao N, Shen Q, Chen J, Hao Z (2013). Facile preparation of 3D ordered mesoporous $CuO_x$–$CeO_2$ with notably enhanced efficiency for the low temperature oxidation of heteroatom-containing volatile organic compounds. RSC Advances, 3(42): 19639–19656

Huang Q, Zuo S F, Zhou R X (2010). Catalytic performance of pillared interlayered clays (PILCs) supported CrCe catalysts for deep oxidation of nitrogen-containing VOCs. Applied Catalysis B: Environmental, 95(3–4): 327–334

Kim K H, Szulejko J E, Kumar P, Kwon E E, Adelodun A A, Reddy P A K (2017). Air ionization as a control technology for off-gas emissions of volatile organic compounds. Environtal Pollution, 225: 729–743

Lai S, Meng D, Zhan W, Guo Y, Guo Y, Zhang Z, Lu G (2015). The promotional role of Ce in Cu/ZSM-5 and in situ surface reaction for selective catalytic reduction of $NO_x$ with $NH_3$. RSC Advances, 5(110): 90235–90244

Li N, Xing X, Sun Y, Cheng J, Wang G, Zhang Z, Hao Z (2020). Catalytic oxidation of *o*-chlorophenol over $Co_2$XAl (X = Co, Mg, Ca, Ni) hydrotalcite-derived mixed oxide catalysts. Frontiers of Environmental Science & Engineering, 14(6): 105

Liu N, Yuan X, Chen B, Li Y, Zhang R (2017). Selective catalytic combustion of hydrogen cyanide over metal modified zeolite catalysts: From experiment to theory. Catalysis Today, 297: 201–210

Liu X, Wang A, Li L, Zhang T, Mou C Y, Lee J F (2011). Structural changes of Au–Cu bimetallic catalysts in CO oxidation: In situ XRD, EPR, XANES, and FT-IR characterizations. Journal of Catalysis, 278(2): 288–296

Liu X, Wu X, Weng D, Shi L (2016). Modification of Cu/ZSM-5 catalyst with $CeO_2$ for selective catalytic reduction of $NO_x$ with ammonia. Journal of Rare Earths, 34(10): 1004–1009

Luo J, Kamasamudram K, Currier N, Yezerets A (2018). $NH_3$-TPD methodology for quantifying hydrothermal aging of Cu/SSZ-13 SCR catalysts. Chemical Engineering Science, 190: 60–67

Ma M, Huang H, Chen C, Zhu Q, Yue L, Albilali R, He C (2018). Highly active SBA-15-confined Pd catalyst with short rod-like micro-mesoporous hybrid nanostructure for *n*-butylamine low-temperature destruction. Molecular Catalysis, 455: 192–203

Ma M, Jian Y, Chen C, He C (2020). Spherical-like Pd/$SiO_2$ catalysts for *n*-butylamine efficient combustion: Effect of support property and preparation method. Catalysis Today, 339: 181–191

Nanba T, Masukawa S, Uchisawa J, Obuchi A (2004). Screening of catalysts for acrylonitrile decomposition. Catalysis Letters, 93(3/4): 195–201

Nanba T, Masukawa S, Uchisawa J, Obuchi A (2007). Mechanism of acrylonitrile decomposition over Cu-ZSM-5. Journal of Molecular Catalysis A Chemical, 276(1–2): 130–136

Nanba T, Masukawa S, Uchisawa J, Obuchi A (2008). Effect of

support materials on Ag catalysts used for acrylonitrile decomposition. Journal of Catalysis, 259(2): 250–259

Pan H, Jian Y, Chen C, He C, Hao Z, Shen Z, Liu H (2017). Sphere-shaped $Mn_3O_4$ catalyst with remarkable low-temperature activity for methyl-ethyl-ketone combustion. Environmental Science & Technology, 51(11): 6288–6297

Pereda-Ayo B, De La Torre U, Illán-Gómez M J, Bueno-López A, González-Velasco J R (2014). Role of the different copper species on the activity of Cu/zeolite catalysts for SCR of $NO_x$ with $NH_3$. Applied Catalysis B: Environmental, 147: 420–428

Wang D, Zhang L, Li J, Kamasamudram K, Epling W S (2014). $NH_3$-SCR over Cu/SAPO-34: Zeolite acidity and Cu structure changes as a function of Cu loading. Catalysis Today, 231: 64–74

Wang J, Tan H, Jiang D, Zhou K (2017). Enhancing $H_2$ evolution by optimizing H adatom combination and desorption over Pd nanocatalyst. Nano Energy, 33: 410–417

Xing X, Li N, Cheng J, Sun Y, Zhang Z, Zhang X, Hao Z (2020). Synergistic effects of Cu species and acidity of Cu-ZSM-5 on catalytic performance for selective catalytic oxidation of *n*-butylamine. Journal of Environmental Sciences-China, 96: 55–63

Xue H, Guo X, Wang S, Sun C, Yu J, Mao D (2018). Poisoning effect of CaO on Cu/ZSM-5 for the selective catalytic reduction of NO with $NH_3$. Catalysis Communications, 112: 53–57

Yashnik S, Ismagilov Z (2015). Cu-substituted ZSM-5 catalyst: Controlling of $DeNO_x$ reactivity via ion-exchange mode with copper–ammonia solution.. Applied Catalysis B: Environmental, 170–171: 241–254

Yashnik S A, Salnikov A V, Vasenin N T, Anufrienko V F, Ismagilov Z R (2012). Regulation of the copper-oxide cluster structure and $DeNO_x$ activity of Cu-ZSM-5 catalysts by variation of $OH/Cu^{2+}$. Catalysis Today, 197(1): 214–227

Zhang R, Li P, Xiao R, Liu N, Chen B (2016a). Insight into the mechanism of catalytic combustion of acrylonitrile over Cu-doped perovskites by an experimental and theoretical study. Applied Catalysis B: Environmental, 196: 142–154

Zhang R, Liu N, Lei Z, Chen B (2016b). Selective transformation of various nitrogen-containing exhaust gases toward $N_2$ over zeolite catalysts. Chemical Reviews, 116(6): 3658–3721

Zhang R, Shi D, Liu N, Cao Y, Chen B (2014). Mesoporous SBA-15 promoted by 3d-transition and noble metals for catalytic combustion of acetonitrile. Applied Catalysis B: Environmental, 146: 79–93

Zhang T, Shi J, Liu J, Wang D, Zhao Z, Cheng K, Li J (2016c). Enhanced hydrothermal stability of Cu-ZSM-5 catalyst via surface modification in the selective catalytic reduction of NO with $NH_3$. Applied Surface Science, 375: 186–195

Zhang X, Gao B, Creamer A E, Cao C, Li Y (2017). Adsorption of VOCs onto engineered carbon materials: A review. Journal of Hazardous Materials, 338: 102–123

Zhao Z, Yu R, Shi C, Gies H, Xiao F S, De Vos D, Yokoi T, Bao X, Kolb U, Mcguire R, Parvulescu A N, Maurer S, Müller U, Zhang W (2019). Rare-earth ion exchanged Cu-SSZ-13 zeolite from organotemplate-free synthesis with enhanced hydrothermal stability in $NH_3$-SCR of $NO_x$. Catalysis Science & Technology, 9(1): 241–251

Zhou J, Xia Q H, Shen S C, Kawi S, Hidajat K (2004). Catalytic oxidation of pyridine on the supported copper catalysts in the presence of excess oxygen. Journal of Catalysis, 225(1): 128–137